

Generation of Transient Dayside Sub-Auroral Proton Precipitation

S. A. Fuselier¹, S. P. Gary², M. F. Thomsen², E. S. Claflin¹, B. Hubert³, B. R. Sandel⁴, and T. Immel⁵

¹Lockheed Martin Advanced Technology Center, Palo Alto, CA

²Los Alamos National Laboratory, Los Alamos, NM

³Université de Liège, Liège, Belgium

⁴Lunar and Planetary Laboratory, The University of Arizona, Tucson, AZ

⁵Space Sciences Laboratory, University of California Berkeley, Berkeley, CA

Abstract: The IMAGE spacecraft obtained the first global images of the proton aurora. One of the discoveries from these images was a region of proton precipitation equatorward of the nominal auroral oval. This precipitation can be observed for approximately 10 minutes immediately following a large solar wind pressure pulse. Various mechanisms have been proposed for producing this precipitation. This study focuses on one of the proposed mechanisms, the scattering and precipitation of protons due to interaction with electromagnetic ion cyclotron (EMIC) waves. Using data from the IMAGE spacecraft FUV and EUV imagers, in situ ring current data from the Los Alamos geosynchronous spacecraft, and in situ solar wind data from the ACE spacecraft, two features of the precipitation - the local time occurrence and limited latitudinal extent - are explained. The local time occurrence of the precipitation is correlated with the orientation of the pressure pulse front in the solar wind. The limited latitudinal extent of the emissions appears to be related to the interaction between the hot ring current protons and the cold plasmaspheric ions that gives rise to EMIC wave growth.

1. Introduction

Although aurora generated by precipitation of energetic (~ 10 's of keV) protons have been observed from the ground [e.g., Ono et al., 1987], the first global images of proton-generated auroral were obtained from the IMAGE spacecraft [Burch, 2000]. This spacecraft was launched into a polar, elliptical orbit in March 2000. During the first three years of observations, the spacecraft apogee precessed over the north geographic pole, providing excellent viewing of the northern auroral region.

The spacecraft has a set of Far Ultraviolet (FUV) imagers which image aurora in several wavelengths [Mende et al., 2000]. These aurora are produced by proton and electron precipitation in the upper atmosphere. The unique ability to make simultaneous images of aurora

created solely by proton precipitation and aurora created by a combination of proton and electron precipitation has produced new results in auroral and magnetospheric physics (see, e.g., Mende et al. [2001]).

One particularly interesting, new discovery is the presence of auroral arcs equatorward of the dayside auroral oval. These auroral arcs have been described as afternoon-sector detached proton auroral arcs [Burch et al., 2002], detached proton arcs [Immel et al., 2002], dayside detached auroras [Zhang et al., 2003], and sub-auroral proton flashes [Hubert et al., 2003]. All of these descriptive terms identify common features of the phenomenon. In particular, the arcs occur equatorward of and separate from the nominal dayside proton auroral oval and they are created entirely from precipitation of protons [Immel et al., 2002; Hubert et al., 2003; Zhang et al., 2003]. (On the dayside, the nominal proton auroral oval is produced by precipitation of protons that originate near the magnetopause.)

The persistence of the sub-auroral proton precipitation suggests two separate categories for the phenomenon. Some arcs persist for many tens of minutes to over an hour [Burch et al., 2002; Immel et al., 2002], while others appear abruptly and fade within 10 minutes of their initial occurrence [Fuselier et al., 2001; Zhang et al., 2003; Hubert et al., 2003]. While the root generation mechanism for the proton precipitation might be the same [e.g., Burch et al., 2002], the different durations suggest that two different processes drive the arc creation.

The initial appearance of the longer duration sub-auroral arcs has been linked to changes in the interplanetary magnetic field (IMF) [Burch et al., 2002]. When the IMF B_z component rotates from southward to northward, the auroral oval contracts toward higher latitudes. Proton precipitation from the ring current may not change latitude, resulting in the appearance of a sub-auroral arc as the auroral oval contracts. An IMF B_y rotation from negative to positive will

produce a similar effect. For this rotation, the oval will shift from dusk to dawn, potentially exposing a sub-auroral proton arc on the duskside. Both IMF orientation changes have been observed to create duskside, long duration sub-auroral arcs [Burch et al., 2002]. The persistence of these arcs on the duskside has been linked to the cold plasmaspheric population on that side of the magnetosphere [Burch et al., 2002; Spasojević et al., 2003].

Shorter duration sub-auroral proton arcs have been associated with rapid increases in the solar wind dynamic pressure either through interplanetary shocks or pressure pulses [Fuselier et al., 2001; Zhang et al., 2003; Hubert et al., 2003]. These transient arcs have several features that suggest their generation mechanism. They occur in association with rapid increases in dynamic pressure [Fuselier et al., 2001], although the initial brightening of the arc can lag the brightening of the auroral oval [Zhang et al., 2003]. They are not confined to the duskside [Hubert et al., 2003]. The arcs are often separated from the auroral oval in latitude, usually by several degrees. Magnetic field lines that are equatorward of the auroral oval map to the equatorial, outer magnetosphere inside the magnetopause. This is the general region of the equatorial ring current and the precipitation in the arc consists entirely of protons with ring current energies [Hubert et al., 2003; Zhang et al., 2003]. The arcs can occur under any solar wind IMF conditions, but they are best observed when the IMF is northward during the increase in dynamic pressure [Hubert et al., 2003].

Several mechanisms have been proposed for the generation of these short duration sub-auroral proton arcs [Hubert et al., 2003; Zhang et al., 2003]. To be consistent with the precipitating proton energy, all proposed mechanisms invoke some sort of pitch angle diffusion of ring current particles into the loss cone through wave-particle interactions. Candidate instabilities include the loss cone instability, field-aligned resonances, and the electromagnetic

ion cyclotron (EMIC) instability [Hubert et al., 2003]. Scattering by EMIC waves is particularly promising because these waves are common in the outer magnetosphere near noon and near dawn, even in the absence of a compression of the magnetosphere [Anderson et al., 1992]. The ring current proton distributions can be near the threshold of the instability [Anderson et al., 1996] and the waves are readily generated during compression events [Anderson and Hamilton, 1993]. Finally, the growth of the instability is suppressed by rapid pitch angle scattering, reducing the anisotropy of ring current protons (i.e., reducing the free energy source of the waves) [Gary et al., 1994; 1995]. This rapid pitch angle scattering will force ring current protons into the atmospheric loss cone.

While promising, the generation of sub-auroral proton arcs through the above EMIC wave-particle mechanism requires some detailed investigation. This or any other generation mechanism must be able to explain two characteristics of these short-duration proton arcs. First, these proton arcs are not confined to the duskside but can occur over a longitudinal extent centered at almost any local time on the dayside. Second, the arcs are often separated from the main auroral oval. This second characteristic implies that there is a gap in the proton precipitation. The protons that produce the dayside auroral oval emissions originate at or near the magnetopause. The occurrence frequency of EMIC waves also peaks close to the magnetopause [Anderson et al., 1992], as does the ring current proton anisotropy [e.g., Sibeck et al., 1987]. In contrast, the sub-auroral arc resides at the ionospheric footpoint of magnetic field lines that cross the equatorial plane in the vicinity of geosynchronous orbit (i.e., well inside the magnetopause). There is little scattering of protons into the loss cone in the gap between the equatorial magnetopause and the mapped location of the sub-auroral arcs. Based solely on the

increasing ring current proton anisotropy with increasing radial distance from the Earth, this gap is difficult to explain using the EMIC waves.

This paper investigates these two features of the short duration sub-auroral proton arcs produced by rapid changes in solar wind dynamic pressure. In Section 2, the instrumentation used in the investigation is briefly described. In Section 3, the IMAGE and solar wind observations are introduced using a single event as an example. In Section 4, the IMAGE and solar wind observations from many events are used to demonstrate how proton arcs can be centered at almost any dayside local time. In Section 5, the aspects of EMIC wave theory relevant to the investigation are described. In Section 6, ring current and plasmasphere observations are introduced and EMIC wave theory is applied to several events to demonstrate how proton arcs can occur detached from the auroral oval. Finally, in Section 7 the observations are summarized and discussed.

2. Instrumentation

Remote sensing auroral observations in this paper are from the Spectrographic Imager SI12 [Mende et al., 2000] on the IMAGE spacecraft. This spectrograph images Doppler-shifted Lyman-Alpha emissions and excludes emissions from the intense, geocoronal Lyman-Alpha line at 121.6 nm. These Doppler-shifted emissions are produced by protons precipitating into the upper atmosphere that charge-exchange with upper atmospheric constituents. The newly created hydrogen atoms are moving away from the spacecraft, so the Lyman-Alpha photons they emit are Doppler-shifted to longer wavelengths. As discussed above, this paper focuses on the dayside precipitation produced by precipitating ring current protons with initial energies ~ 10 keV.

Remote sensing plasmaspheric observations are from the Extreme Ultraviolet (EUV) cameras [Sandel et al., 2000] on the IMAGE spacecraft. These cameras produce images of 30.4 nm solar radiation that is resonantly scattered off of plasmaspheric He^+ . The observed 30.4 nm intensity is a line-of-sight integral measure of the plasmaspheric He^+ .

In situ ring current and plasmaspheric observations are from the Magnetospheric Plasma Analyzers (MPA) [Bame et al., 1993] on the Los Alamos National Laboratory geosynchronous spacecraft. These electrostatic analyzers measure ion and electron distributions with energies from the spacecraft potential to about 40 keV/e. The ion data are used to determine the in situ growth rate of EMIC waves at geosynchronous orbit, occasionally for several local times (using data from several spacecraft). To determine the growth rate of the waves, the hot proton temperature anisotropy, the plasma β (the ratio of particle energy to the magnetic field energy), and the cold plasma density are needed. Although there are no magnetometers on the spacecraft, the hot proton temperatures perpendicular and parallel to the background magnetic field direction are determined from the fully 3-dimensional ion data and the assumption of gyrotropy. The directions perpendicular and parallel to the background magnetic field obtained from the ion observations are checked using the simultaneous electron observations (since electrons are also anisotropic in the outer magnetosphere). To determine the plasma β , the densities and temperatures from the electrostatic analyzers are used and magnetic field magnitude is estimated from the nearest GOES spacecraft (also in geosynchronous orbit). One of the features of the LANL MPA instruments is that they typically float at a negative potential. Thus, the electrostatic analyzers also measure the in situ cold plasmaspheric ion population (with typical energies below 1 eV/e).

Finally, in situ solar wind plasma and magnetic field observations are from the solar wind electron proton alpha monitor (SWEPAM) and the magnetic fields experiment on the ACE spacecraft. This spacecraft is located in the solar wind at the L1 Lagrange point (approximately $237 R_E$ upstream from the Earth), resulting in time delays for solar wind propagation to the Earth's magnetopause of ~ 50 min.

3. Sub-Auroral Proton Arc Example on 25 October 2001

Figures 1 and 2 show one hour of data from the ACE spacecraft from 25 October 2001. In Figure 1, data from the ACE magnetic fields experiment [Smith et al., 1998] are shown and in Figure 2, data from the ACE SWEPAM [McComas et al., 1998] are shown. At 0802 UT, the ACE spacecraft observed the passage of a strong interplanetary shock. Across this shock, the magnetic field increased and rotated (Figure 1) and the density and velocity increased (Figure 2). The dramatic increase in the solar wind density and the increase in the velocity resulted in a solar wind dynamic pressure increase of a factor of 5.5. From the ACE spacecraft location at the L1 point, the interplanetary shock propagated to the Earth's magnetopause in approximately 50 min. The magnetopause was compressed and effects of this compression were seen in the ionosphere starting at about 0853 UT.

Figure 3 shows observations from the IMAGE spacecraft on 25 October 2001 and illustrates typical features of the sub-auroral proton arcs associated with dramatic increases in solar wind dynamic pressure. The top panels of Figure 3 show the proton auroral emissions from the SI12 imager remapped into geomagnetic coordinates (Invariant latitude and Magnetic Local Time (MLT)). The view is from over the north magnetic pole with noon at the top and dusk to the left.

The bottom panels show how these emissions map to the equatorial plane (see below). The color bars for the top and bottom panels are different and were chosen to highlight features in panels.

The first effects of the interplanetary shock were seen in the ionosphere at 0853 UT (just before the first image in Figure 3) as a brightening of the auroral oval. In the first image at 0855 UT in Figure 3, the sub-auroral proton emissions are seen between about 11 and 15 MLT and between 65° and 70° invariant latitude. There is a clear separation between the sub-auroral arc, which peaks at about 68° invariant latitude and the dayside auroral oval, which peaks at about 75° invariant latitude near noon (12 MLT). In subsequent images in Figure 3, the sub-auroral emissions move in both local time and latitude. At 0857 UT, the emissions have split so that there are two arcs extending from 9 to about 11 MLT and from 12 to about 16 MLT. The duskside arc has moved to higher latitude and closer to the auroral oval. A gap between the sub-auroral emissions and the auroral oval is no longer discernable, except from about 15 to 16 MLT. By 0859 UT, the separation between the dawnside and duskside arcs has increased and these arcs have merged with the auroral oval. The duskside arc has a greater invariant latitude extent and is more intense than the dawnside arc. In the next two images (not shown) the sub-auroral emissions fade and are gone by 0905 UT.

In the bottom panels in Figure 3, the emissions between 60° and 80° invariant latitude are mapped to the equatorial plane. To produce the mapped images, the corners of each pixel in this invariant latitude range were mapped from the ionosphere (assuming emissions at 100 km altitude) to the equatorial plane in the Tsygenanko 96 [Tsygenanko, 1995] model. The outer limit of the mapping from the high latitude ionosphere to the equatorial plane is the magnetopause, which is compressed by the interplanetary shock from its nominal standoff distance of about $10 R_E$. The oval shaped inner boundary in the bottom panels of Figure 3 is

created by limiting the mapping to invariant latitudes greater than 60° . The auroral oval at 12 MLT maps tailward of $-20 R_E$ on lobe field lines (which will be reconnected at high latitudes, forming the cusp [e.g., Fuselier et al., 2002]). The duskside auroral oval between 70° and 75° invariant latitude and between 15 and 18 MLT maps to the duskside magnetopause just tailward of the terminator. In general, dayside pixels map to the dayside equatorial region with relatively little distortion, an indication that small changes in latitude result in correspondingly small changes in radial distance from the Earth. In contrast, pixels on the nightside map with significant distortion.

In the bottom left hand panel of Figure 3 (corresponding to the FUV image at 0855 UT), the sub-auroral proton emissions are between 11 and 15 MLT and between 5.5 and $8 R_E$. There is a clear peak in the emissions that occurs on the duskside, between the magnetopause and the inner boundary of the mapping. This peak is located near geosynchronous orbit ($6.6 R_E$). In the mapping of the image at 0857 UT, the sub-auroral emissions split, move to earlier and later magnetic local times, and closer to the magnetopause. By 0859 UT, the duskside emissions have merged with the magnetopause emissions, forming a broad region of emissions extending earthward from the magnetopause several R_E and from about 14 to 18 MLT. The fainter dawnside emissions have merged with the magnetopause between 8 and 11 MLT.

Although the splitting and propagation of the sub-auroral emissions are features not discussed previously, the other features of the sub-auroral emissions shown in Figure 3 have been reported [Hubert et al., 2003; Zhang et al., 2003]. In particular, the emissions are not confined to the duskside, they are clearly separated from the auroral oval (at least initially), they appear approximately in association with the arrival of a solar wind dynamic pressure pulse, and they last of the order of 10 minutes.

4. Local Time Dependence of Sub-Auroral Emissions

The sub-auroral emissions in Figure 3 initially appear on the duskside. Similar events with peak emissions occurring initially at noon and on the dawnside have been reported previously [Hubert et al., 2003]. To investigate the local time occurrence of the emissions, solar wind data from ACE and IMAGE data were surveyed from June 2000 (shortly after science operations began on IMAGE) to October 2002. During this period, there were 18 interplanetary shocks similar to the one shown in Figures 1 and 2 that had associated sub-auroral emissions like those in Figure 3. There were more interplanetary shocks and other sudden increases in dynamic pressure in the solar wind during this period. Not all of these sudden increases in solar wind dynamic pressure had sub-auroral emissions associated with them (see also Zhang et al. [2003]). Although interesting and potentially important for understanding the creation of these sub-auroral emissions, the association between the type of solar wind disturbance and presence or absence of sub-auroral emissions is not considered here. Rather, the focus here is on interplanetary shocks (where the shock normal can be computed) that are associated with sub-auroral emissions. Table 1 lists the 18 interplanetary shocks used in this study.

Shock normals were computed for the 18 shocks in Table 1 using the minimum variance technique (e.g., Seon, 1998). Figure 4 compares the orientation of the shock normal with respect to the GSM x-y plane (keeping the x direction of the normal positive, toward the Sun) to the location of the peak emissions in the sub-auroral arcs mapped to the GSM equatorial plane. Although there is not a strong correlation between these two angles, there is a clear preference for sub-auroral arcs to peak on the duskside (dawnside) when the shock normal has a positive (negative) Y_{GSM} component. The example in Figure 3 is included in Table 1 and in Figure 4.

For this event, the shock normal in the x-y GSM plane was at an angle of $+35^\circ$ relative to the Earth-Sun line (i.e., the shock arrived on the duskside of the magnetopause first) and the sub-auroral emissions in the bottom left-hand panel of Figure 3 peak on the duskside at 24° relative to the Earth-Sun line.

5. EMIC Wave Theory

Figure 4 suggests that the initial local time occurrence of the sub-auroral emissions is determined entirely by properties of the pressure pulse or shock in the solar wind. Thus far, EMIC waves have not been invoked as a mechanism for the precipitation of the protons responsible for creating the sub-auroral emissions. In this section, relevant aspects of EMIC wave theory are introduced in anticipation of their use in Section 6, where the latitudinal extent of the emissions is investigated.

The Electromagnetic Ion Cyclotron (EMIC) instability is driven by the temperature anisotropy ($A_h = T_{\perp h}/T_{\parallel h} - 1$) of the hot, ring current proton distribution in the outer magnetosphere. In the duskside magnetosphere, a process known as drift shell splitting causes these proton distributions to become increasingly anisotropic as they propagate from the nightside around the duskside to the dayside [e.g., Sibeck et al., 1987]. In drift shell splitting, protons with small pitch angles preferentially drift to lower L shells on the dayside while those with large pitch angles drift to higher L shells. The result is a proton population whose anisotropy increases with increasing L shell in the subsolar and duskside magnetosphere. Compression of the magnetosphere due to the arrival of a solar wind pressure pulse should enhance this anisotropy to some degree throughout the dayside magnetosphere [Anderson and Hamilton, 1993].

The proton temperature anisotropy is the free energy source for the EMIC instability. This instability has maximum growth rate at propagation parallel or antiparallel to the background magnetospheric magnetic field, so that protons are predominantly pitch angle scattered by the wave. Wave-particle interactions strongly scatter particles only when the anisotropy is sufficiently strong to excite the instability. This pitch angle scattering acts to reduce the free energy source and, when the anisotropy is reduced below a certain level, the instability is quenched.

The theory for EMIC linear growth and the nonlinear saturation of the instability have been investigated in detail and are summarized in Gary et al. [1994]. Assuming a magnetospheric plasma consisting of a tenuous ($\sim 1 \text{ cm}^{-3}$), hot (several keV), anisotropic ($T_{\perp h}/T_{\parallel h} \sim 2$) proton population and a relatively dense ($\sim 10 \text{ cm}^{-3}$), cold ($\sim 1 \text{ eV}$), isotropic proton population, the threshold condition for the cyclotron instability is written as:

$$A_h = T_{\perp h}/T_{\parallel h} - 1 = S_h / (\beta'_h)^{-h} \quad \text{Equation 1}$$

Where $A_h = T_{\perp h}/T_{\parallel h} - 1$ is the temperature anisotropy of the hot, tenuous proton population, β'_h is a modified form of the hot plasma beta (the ratio of plasma thermal energy to magnetic energy) $= 8\pi n_h T_{\parallel h}/B_o$ (n_e is the total density $= n_c + n_h$, and B_o is the background magnetic field magnitude), $\beta_h \approx 0.4$ and the fitting parameter $S_h \sim 1$ is a function of the growth rate at threshold as well as of n_h / n_c [Gary et al., 1994; 1995]. The parameter β'_h is used instead of the usual form of the plasma beta, $\beta_{\parallel h} = 8\pi n_h T_{\parallel h}/B_o$, because the threshold is less sensitive to changes in the hot proton relative density when plotted as a function of β'_h over the range of density ratios $0.01 <$

$n_h/(n_c + n_h) < 1$. This range will be shown to adequately cover the observed values for the events in the next section.

Computer simulations [Gary et al., 1994; 1995] show that, if the hot protons are given an initial anisotropy well above the instability threshold, pitch angle scattering by the enhanced fluctuations will rapidly reduce the anisotropy to the threshold condition. Subsequent scattering further reduces this quantity much more slowly. Given the results from these simulations, the EMIC wave mechanism produces proton precipitation through the following scenario. Ring current proton distributions in the outer magnetosphere are at or near threshold [Anderson et al., 1996]. The arrival of a sharp solar wind pressure pulse causes the magnetosphere to be compressed, which suddenly raises the growth rate of the EMIC instability to a value well above instability threshold. The EMIC waves grow rapidly and, through wave particle interactions, the protons are scattered into the loss cone and precipitate into the atmosphere.

The location of the precipitation in the ionosphere depends critically on how and where the growth rate of the EMIC instability increases in the equatorial outer magnetosphere. According to Equation 1, the growth rate at threshold, S_h , (and therefore the growth rate of the instability) depends directly on A_h and $\beta_h = 8\pi n_e T_{\parallel h} / B_o$ (where $n_e = n_c + n_h$). In an adiabatic compression of the magnetosphere, the temperature anisotropy, density, perpendicular temperature, and magnetic field can all increase. It is the competition between these factors that will determine where in the equatorial magnetosphere the EMIC instability will go unstable, rapidly scatter particles into the loss cone, and produce ionospheric precipitation.

6. Radial Dependence of Sub-Auroral Emissions

To investigate the relative importance of changes in A_h and α_h in the growth of EMIC waves in the magnetosphere, in situ measurements of the ring current and plasmasphere from the Los Alamos geosynchronous spacecraft are used (and, for the magnetic field magnitude, the magnetometer measurements from the nearest GOES spacecraft are used).

One of the important assumptions in the derivation of Equation 1 is that the outer magnetospheric plasma consists of two populations, a hot, ring current component and a cold, plasmaspheric population. Typically, proton distributions in the outer magnetosphere are more complex, often consisting of two or more hot components with different characteristic energies [e.g., Anderson et al., 1996]. The lower energy component has a temperature of ~ 10 - 20 keV/e while the higher energy component can have temperatures above 40 keV/e. Despite its lower density when compared to that of the lower energy component, the higher energy proton component can contribute as much as half of the total growth rate of the EMIC instability [Anderson et al., 1996].

The MPAs on the Los Alamos spacecraft measure ion energies (E/Q) from the spacecraft potential to 40 keV/e. Thus, the analyzers cover well the cold population and the lower energy ring current component. The higher energy component is measured by the Synchronous Orbit Particle Analyzers (SOPAs) on the spacecraft. Unfortunately, the temperature anisotropy is not a normal data product derived from these energetic particle telescopes.

By computing A_h and α_h using only the lower energy component of the proton distribution measured by the MPAs, the absolute value of the growth rate of the EMIC waves could be underestimated by about a factor of 2. However, the interest here is on the relative changes in A_h and α_h and the growth rate as the magnetosphere is compressed by an interplanetary shock or pressure pulse. Thus, as long as the higher energy proton component does not change

dramatically during the compression of the magnetosphere, the relative changes in A_h and $_{h}$ will be reasonably well determined from the MPA data.

To minimize the effect of the higher energy proton component on the relative changes in A_h and $_{h}$, events were selected where the total energetic (from 50 - 200 keV/e) proton fluxes had little variation (less than a factor of 2) before and after the magnetospheric compression.

Table 2 shows 11 events used to test the EMIC wave mechanism and the relative importance of changes in A_h and $_{h}$. To identify a candidate event, sub-auroral proton arcs were mapped from the ionosphere to the equatorial magnetosphere using the same procedure described in Section 3 that produced the mapping of the 25 October 2001 event (Figure 3). The locations of the Los Alamos geosynchronous spacecraft were checked to determine if any were in the mapped precipitation region. If data were available in the mapped region, then the higher energy proton data were checked to make sure the total flux above 50 keV did not change by more than a factor of 2. The 25 October 2001 compression event was particularly good in all aspects because there were three Los Alamos spacecraft located at different local times (Table 2) and all were in the broad region of precipitation observed over the 10-minute lifetime of the event (Figure 3). These observations were considered as separate events in Table 2, even though they come from the same magnetospheric compression interval.

Using the plasma conditions ten minutes before the compression and immediately following the compression observed at the Los Alamos spacecraft, A_h , $_{h}$, and the threshold condition (Equation 1) were computed. The MPA data has a resolution of 1 min and, unless there were significant fluctuations in the density and/or temperature before or immediately after the compression, the highest time resolution data were used. If there were significant fluctuations in these parameters, then a 3-spectrum average was used.

Figure 5 shows the results of this computation for the events in Table 2. Plotted are A_h and ω_{pe} before (\square 's) and after (\bullet 's) the magnetospheric compression. For each event, a dashed line connects the conditions before with those after the compression. The solid line in Figure 5 shows the nominal marginal stability lines for the EMIC instability. These marginal stability lines are defined as the locus of points where the ratio of the growth rate to the proton cyclotron frequency, $\gamma / \omega_{cp} = 0.001$ [see Gary et al., 1994; Anderson et al., 1996]. The two lines shown are for $n_h / (n_h + n_c) = 0.02$ and $= 0.4$ and represent the extreme values of this ratio for the 11 events in Table 2. Plasma populations with A_h and ω_{pe} well above these lines are highly unstable to EMIC waves.

Most of the events in Figure 5 support the EMIC wave generation mechanism described in the previous Section. For 10 of the 11 events, the change in plasma conditions led to an increase in the instability growth, as shown in the comparison of the two columns representing the growth rates in Table 2. For only one event, the relative change in the growth rate was small and in the direction of increasing stability.

While Figure 5 and Table 2 support the EMIC wave generation mechanism, they do not necessarily provide information on the relative importance of A_h and ω_{pe} in determining the EMIC instability growth rate. To understand the relative importance of these two parameters in local control of the EMIC instability (that is, before and after the magnetospheric compression observed at the Los Alamos geosynchronous spacecraft), a systematic study was done on the ten cases where the growth rate increased as a result of the compression.

In this systematic study, one parameter was held constant at its value before the magnetospheric compression while the other parameter was changed to match the value observed after the magnetospheric compression. The result of this analysis showed that the change in A_h

makes the largest contribution to the increase in the growth rate in 6 of the 10 events. In the other four events, it was the increase in β_h that made the largest contribution to the growth rate. However, even for these 4 events, it was the change in n_h and not the change in n_c that resulted in the largest contribution to the increase in the growth rate. Thus, locally at the Los Alamos spacecraft, the change in the cold plasma density did not contribute to the growth rate increase.

Although the change in the cold plasma density does not contribute to the growth rate increase locally, the radial profile of the cold plasma density in the magnetosphere may play a significant role in determining the radial extent of the region where the EMIC waves are unstable. Typically, there is significant cold plasma at intermediate distances from the Earth (e.g., near geosynchronous orbit) and the cold plasma density decreases rapidly at the plasmopause, further from the Earth. Such a density profile might cause the EMIC instability to be driven above marginal stability at intermediate distances from the Earth and not further from the Earth, even though the temperature anisotropy in the dayside outer magnetosphere increases with increasing radial distance from the Earth and this anisotropy is the most important quantity in determining the EMIC growth rate. The limited region of precipitation resulting from the control of the EMIC instability by the cold plasma density would produce a sub-auroral arc that is separated from the auroral oval, as in Figure 3.

To test this hypothesis, a second systematic study was performed on the 10 events in Figure 5 where the growth rate increased after the magnetospheric compression. For this study, A_h and n_h were fixed at their values observed by the Los Alamos spacecraft after the magnetospheric compression and n_c was changed from its value after the compression to a value between 5 and 10 times smaller. In all 10 cases, the growth rate decreased below the threshold of the instability. An example of this change for one of the events is shown in Figure 6. This parametric study

indicates that, if A_h and n_h were constant with increasing radial distance from the Earth, then the plasma would be stable if the plasmapause was between the observation point at geosynchronous orbit and the magnetopause. To be sure, A_h should increase with increasing radial distance from the Earth. However, this increase is probably not as large as the factor of 5 to 10 decrease in the cold plasma density across the plasmapause. Furthermore, in this parameter regime, a linear increase in A_h results in a linear increase in the EMIC growth rate, while a linear decrease in n_c results in an exponential decrease in the growth rate (Figure 6). Therefore, it is likely that the gap in precipitation often seen between geosynchronous orbit and the magnetopause is produced by the cold plasma density profile.

The cold plasma density profile is observable using the IMAGE Extreme Ultraviolet (EUV) telescopes image the Earth's cold plasmaspheric He^+ . These telescopes have produced the first global images of the Earth's plasmasphere [Sandel et al., 2001]. While these images provide the radial profile of the cold plasma density, there are two difficulties with applying these images to the study of sub-auroral arcs. The first difficulty is that the time resolution of the EUV images are 10 min. Since the time resolution is of the same order as the duration of the sub-auroral proton arc, it is not possible to compare the plasmasphere before and during the sub-auroral proton arc event. The second difficulty is that the 30.4 nm emissions are relatively weak at large distances from the Earth.

Due to the weak 30.4 nm emissions, it is usually not possible to obtain accurate cold plasma densities at L shells beyond about 6-7 R_E under nominal magnetospheric conditions. Thus, the radial profiles of the cold plasma density obtained by EUV typically do not extend into the gap region between the magnetopause and geosynchronous orbit.

Fortunately for this study, sub-auroral proton arcs are observed at very low latitudes on occasion, with a significant gap between the arc and the auroral oval emissions [Hubert et al., 2003]. For these relatively rare events, the region in the equatorial plane where protons are pitch angle scattered into the loss cone is at low L shells (i.e., very close to the Earth) and the gap, where scattering is not occurring, can be inside geosynchronous orbit. The left-hand panels of Figure 7 show such an event. The top two panels have the same format as Figure 3. For the event in the left-hand panels of Figure 7 (16 June 2000), the sub-auroral arc extends to nearly 60° on the dawnside and the gap between the emissions and the auroral oval is as large as 10° at 12 MLT. When mapped to the equatorial magnetosphere, this sub-auroral arc is $\sim 2 R_E$ from the Earth and extends only to about $5 R_E$ at 12 MLT. The result is a gap of nearly $4 R_E$ between the outer edge of the mapped sub-auroral arc and the subsolar magnetopause. Finally, the bottom left-hand panel in Figure 7 compares the radial profile (centered at 12 ± 0.5 MLT) of the mapped FUV emissions with the EUV brightness. There is a decrease in the cold plasma density (i.e., the plasmopause) at about $3.8 R_E$. Similarly, the mapped FUV emissions decrease between 4 and $4.5 R_E$, or in the vicinity of the cold plasma density decrease. That is, within the resolution of the mapping and image, the outer edge of the mapped region of FUV emissions is associated with the decrease in the cold plasma density, identified as the plasmopause. (The plasmasphere for this event is located unusually close to the Earth, as are the mapped sub-auroral proton emissions. The final, relatively sharp decrease at $L=6$ in the EUV brightness is the edge of the EUV image and illustrates the difficulty in using these images to study more typical sub-auroral proton arcs that map to the vicinity of geosynchronous orbit.)

For this event, there were no Los Alamos geosynchronous spacecraft in the mapped emission region. However, one spacecraft was located at 16.9 MLT, outside the mapped emission region

on the duskside. At this duskside location, both A_h and β_h decreased when the magnetosphere was compressed. That is, the plasma in the vicinity of geosynchronous orbit on the duskside became more stable to the growth of EMIC waves. Also, the cold plasma density decreased during the magnetospheric compression, again indicating that, on the duskside in the vicinity of geosynchronous orbit, the plasma was stable to EMIC wave growth.

The cold plasma does not always have a relatively steep gradient in the outer magnetosphere. The right-hand panels of Figure 7 show a similar FUV-EUV comparison for an event on 18 April 2001 where the sub-auroral proton arc was not separated from the auroral oval. In this case, there is no gap between the magnetopause and the FUV intensity decreases rapidly with decreasing L shell. The EUV intensity decreases smoothly with increasing L shell until about 6 R_E , where the poor statistics make it difficult to detect a sharp decrease in cold plasma density that might indicate the plasmapause. In this event, the region of FUV emissions and the cold plasma density appear almost anticorrelated.

For this event, a Los Alamos geosynchronous spacecraft was in the mapped region of the emissions and relatively close to the magnetopause due to the magnetospheric compression. The 18 April 2001 entry in Table 2 shows that the anisotropy was unchanged after the magnetospheric compression. However, β_h increased, moving the plasma toward increasing instability. This event was one of the 4 in Table 2 where the change in n_h caused the increase in the EMIC growth rate. Thus, for this event, it was the increase in the hot plasma density and the hot plasma parallel temperature that caused β_h to increase and the marginal stability condition of the EMIC instability to be exceeded. No sharp gradient was seen in the cold plasma density in the outer magnetosphere and the arc was not separate from the auroral oval.

7. Discussion and Conclusions

In this paper, the solar wind and magnetospheric drivers for two features of sub-auroral proton arcs were investigated. For the first feature – the local time occurrence in the peak of the sub-auroral emissions – the orientation of the solar wind pressure pulse or shock front plays an important role. Figure 3 shows that the orientation of the shock front is associated with the side of the magnetosphere where the peak of the mapped sub-auroral emissions is located. The correlation is far from perfect, but shock fronts that impact the duskside (dawnside) magnetosphere first tend to produce regions of enhanced pitch angle scattering on the duskside (dawnside).

There could be several reasons why the correlation is not perfect. The relatively short duration of the sub-auroral arcs and their propagation to later and earlier local times (Figure 3) could reduce the correlation between the shock front and the local time occurrence of the peak in the emissions. Since the FUV imager makes a ~ 5 -10 sec snapshot of the auroral emissions every 2 minutes and the events typically last only 10 min, the initial precipitation may be missed and the sub-auroral arc might have already moved to earlier (or later) local times by the time the first image is obtained. For example, the peak intensity of the emissions in Figure 3 moves almost 1 hour in magnetic local time (i.e., 15°) from the first to the second consecutive image.

Another reason why the correlation might not be perfect is the uncertainty in the shock normal angle. The minimum variance technique is correctly applied using asymptotic conditions upstream and downstream from the shock. However, the precipitation occurs over a short time period in the first ~ 10 min of the shock arrival at the magnetopause. The orientation of the downstream field just after the shock arrival is typically somewhat different from the asymptotic

orientation (see Figure 1). It is estimated that this can contribute to uncertainties in the shock normal angle of the order of $\pm 20^\circ$.

Finally, the correlation in Figure 4 might not be perfect because of the asymmetric distribution of cold plasma and hot proton anisotropy in the dayside magnetosphere. Figure 4 shows that it is sometimes the case that the sub-auroral proton arcs occur on the duskside, even when the interplanetary shock arrives first on the dawnside. There is no corresponding tendency for arcs on the dawnside when the interplanetary shocks arrive first on the duskside. Figure 3 shows that, as the emissions propagate around the magnetosphere, the dawnside emissions tend to fade more rapidly than the duskside emissions.

Two effects favor EMIC wave growth on the duskside when compared to the dawnside. First, the cold plasma is typically further away from the Earth on the duskside, resulting in a region of higher EMIC growth rate further from the Earth on the duskside. Second, even in the absence of a magnetopause compression, the hot ring current proton anisotropy peaks on the duskside near the magnetopause [e.g., Anderson et al., 1996]. Combining this duskside preference with the possibility that the initial peak in the emissions might be missed by the FUV imager suggests that there is a higher probability of observing a peak in the emissions on the duskside than on the dawnside.

The cold plasma density in the magnetosphere also appears to play an important role in the second feature of sub-auroral proton arcs – the latitudinal extent and the gap between the sub-auroral arc and the main auroral oval. The cold plasma density affects the EMIC waves that grow in response to the magnetospheric compression by increasing ω_h and by lowering the threshold of the instability. In Table 2 there are 10 events where the EMIC growth rate increased after the magnetospheric compression. In all of these events, it was either the increase in A_h or

the increase in n_h that caused the growth rate to increase. However, a decrease in the cold plasma density to a value between 5 and 10 times below that observed after the compression would result in quenching of the EMIC instability, as shown in Figure 6.

These results indicate that the distribution of cold plasma in the outer magnetosphere will strongly influence the locations in the magnetosphere where the precipitation will be initiated. The bottom left hand panel of Figure 7 illustrates this importance. It shows that the gap between the mapped proton precipitation and the magnetopause is related to the drop of the cold plasma density at the plasmopause. Thus, even though the hot plasma anisotropy increases with radial distance from the Earth [e.g., Sibeck et al., 1987], the gap in the precipitation occurs because β_h is higher inside the plasmasphere than outside the plasmasphere.

The cold plasma density does not dominate the EMIC wave growth for all cases. The right hand panels of Figure 7 show such an example. When there is no gap between the sub-auroral proton arc and the auroral oval, the mapped emissions appear to be anti-correlated with the cold plasma density profile. For this event, the geosynchronous spacecraft observations (the 18 April 2001 entry in Table 2) in the region of the mapped emissions showed that the EMIC wave growth rate increased because of an increase in β_h primarily through an increase in the hot plasma density.

These results suggest that the gap between the sub-auroral arcs and the auroral oval is directly related to the presence of a plasmopause in the outer magnetosphere. Even though the temperature anisotropy increases with increasing radial distance from the Earth [Sibeck et al., 1987; Anderson et al., 1992; Anderson and Hamilton, 1993], the decrease in the cold plasma density at the plasmopause typically determines the sunward extent of the precipitation region for the sub-auroral proton emissions.

A similar EMIC wave mechanism for producing long duration sub-auroral proton arcs has been suggested [Burch et al., 2002]. In this instance, the sub-auroral proton arc on the duskside is exposed by a rotation of the interplanetary magnetic field. These arcs have a duration on the order of an hour. Consistent with the importance of the cold plasma density in the generation of EMIC waves, it has recently been demonstrated that the sunward edge of a long duration sub-auroral proton arc is closely associated with the plasmaspheric plume on the duskside [Spasojević et al., 2003]. Thus, the location of sub-auroral proton arcs appears to be controlled by the cold plasma density in the outer magnetosphere independent of their duration.

Acknowledgements: The success of the IMAGE mission is a tribute to the many dedicated scientists and engineers that have worked and continue to work on the project. The PI for the mission is Dr. J. L. Burch. ACE observations in this paper are from the NASA CDAWeb. N. Ness at Bartol Research Institute and D. J. McComas at Southwest Research Institute provided these data. Research at Lockheed Martin was supported through an IMAGE subcontract from the University of California Berkeley. Work at Los Alamos was conducted under the auspices of the US Department of Energy, with partial support from NASA Sun-Earth Connections Theory Program. The authors thank the referee for insightful comments on the theoretical aspects of EMIC wave growth.

References

- Anderson, B. J., and D. C. Hamilton, Electromagnetic ion cyclotron waves stimulated by modest magnetospheric compressions, *J. Geophys. Res.*, 98, 11,369, 1993.
- Anderson B. J., R. E. Earlandson, and L. J. Zanetti, A statistical study of Pc 1-2 magnetic pulsations in the equatorial magnetosphere, 1, Equatorial occurrence distributions, *J. Geophys. Res.*, 97, 3075, 1992.

- Anderson, B. J., R. E. Denton, G. Ho, D. C. Hamilton, S. A. Fuselier, and R. J. Strangeway, Observational test of local proton cyclotron instability in the Earth's magnetosphere, *J. Geophys. Res.*, *101*, 21,527-21,543, 1996.
- Bame, S. J., D. J. McComas, M. F. Thomsen, B. L. Baraclough, R. C. Elphic, J. P. Glore, J. T. Gosling, J. C. Chavez, E. P. Evans, and F. J. Wymer, Magnetospheric plasma analyzer for spacecraft with constrained resources, *Rev. Sci. Instr.*, *64*, 1026, 1993.
- Burch, J. L., IMAGE mission overview, *Space Sci. Rev.*, *91*, 1, 2000.
- Burch, J. L., et al., Interplanetary magnetic field control of afternoon-sector detached proton auroral arcs, *J. Geophys. Res.*, *107*(A9), 1251, doi:10.1029/2001JA007554, 2002
- Fuselier, S. A., A. G. Ghielmetti, T. E. Moore, M. R. Collier, J. M. Quinn, G. R. Wilson, P. Wurz, S. B. Mende, H. U. Frey, C. Jamar, J.-C. Gerard, J. L. Burch, Ion outflow observed by IMAGE: Implications for source regions and heating mechanisms, *Geophys. Res. Lett.*, *28*, 1163-1166, 2001.
- Fuselier, S. A., H. U. Frey, K. J. Trattner, S. B. Mende, and J. L. Burch, Cusp aurora dependence on interplanetary magnetic field Bz, *J. Geophys. Res.*, *107*(A7), 1111, doi: 10.1029/2001JA900165, 2002.
- Gary, S. P., M. B. Moldwin, M. F. Thomsen, D. Winske, and D. J. McComas, Hot proton anisotropies and cool proton temperatures in the outer magnetosphere, *J. Geophys. Res.*, *99*, 23,603, 1994.
- Gary, S. P., M. F. Thomsen, L. Yin, and D. Winske, Electromagnetic proton cyclotron instability: Interactions with magnetospheric protons, *J. Geophys. Res.*, *100*, 21,961, 1995.
- Hubert, B., J. C. Gérard, S. A. Fuselier, and S. B. Mende, Observation of dayside subauroral proton flashes with the IMAGE-FUV imagers, *Geophys. Res. Lett.*, *30*(3), 1145, doi:10.1029/2002GL016464, 2003.
- Immel, T. J., S. B. Mende, H. U. Frey, L. M. Peticolas, C. W. Carlson, J.-C. Gearad, B. Hubert, S. A. Fuselier, and J. L. Burch, Precipitation of auroral protons in detached arch, *Geophys. Res. Lett.*, *29*(11), 1519, doi:10.1029/2001GL013847, 2002.
- McComas, D. J., S. J. Bame, P. Barker, W. C. Feldman, J. L. Phillips, P. Riley, and J. W. Griffiee, Solar wind electron proton alpha monitor (SWEPAM) for the Advanced Composition Explorer, *Space Sci. Rev.*, *86*, 563, 1998.
- Mende, S. B., et al., Far ultraviolet imaging from the IMAGE spacecraft, 3, Spectral imaging of Lyman- α and OI 135.6 nm, *Space Sci. Rev.*, *91*, 287, 2000.

- Mende, S. B., et al., Global observations of proton and electron auroras in a substorm, *Geophys. Res. Lett.*, **28**, 1139, 2001.
- Ono, T., T. Hirasawa, and C. I. Meng, Proton auroras observed at the equatorward edge of the duskside auroral oval, *Geophys. Res. Lett.*, **14**, 660, 1987.
- Sandel, B. R., et al., The extreme ultraviolet imager investigation for the IMAGE mission, *Space Sci. Rev.*, **91**, 197, 2000.
- Sandel, B. R., R. A. King, W. T. Forrester, D. L. Gallagher, A. L. Broadfoot, and C. C. Curtis, Initial results from the IMAGE extreme ultraviolet imager, *Geophys. Res. Lett.*, **28**, 1439, 2001.
- Seon, J., Determination of normal vectors for boundaries of plasmas based upon Rankine-Hugoniot relations estimated with a single spacecraft, *J. Astron. Space Sci.*, **15**, 11, 1998.
- Sibeck, D. G., R. W. McEntire, A. T. Y. Lui, R. E. Lopez, and S. M. Krimigis, Magnetic field drift shell splitting: Cause of unusual dayside particle pitch angle distributions during storms and substorms, *J. Geophys. Res.*, **92**, 13,485, 1987.
- Smith, C. W., M. H. Acuna, L. F. Burlaga, J. L. Heures, N. F. Ness, J. Scheifele, The ACE magnetic fields experiment, *Space Sci. Rev.*, **86**, 611, 1998.
- Spasojević, M., H. U. Frey, M. F. Thomsen, S. A. Fuselier, B. R. Sandel, and U. S. Inan, The link between a detached sub-auroral proton arc and a plasmaspheric plume, *Geophys. Res. Lett.*, submitted, 2003.
- Tsyganenko, N. A., Modeling the Earth's magnetospheric magnetic field confined within a realistic magnetopause, *J. Geophys. Res.*, **100**, 5599, 1995.
- Zhang, Y., L. J. Paxton, T. J. Immel, H. U. Frey, and S. B. Mende, Sudden solar wind dynamic pressure enhancements and dayside detached auroras: IMAGE and DMSP observations, *J. Geophys. Res.*, **108**(A4), 8001, doi:10.1029/2002JA009355, 2003.

Table 1. Data for 18 interplanetary shocks observed by the ACE spacecraft that were associated with sub-auroral proton arcs observed by the IMAGE spacecraft.

Date	Shock Arrival Time at the ACE Spacecraft (UT)	Shock X-Y GSM angle (degrees) (positive angles – duskside, negative angles – dawnside)	Sub-Auroral Arc Center (degrees) (positive angles – duskside, negative angles – dawnside)
8 June 2000	0840:30	10.3	30
23 June 2000	1226:00	89.5	60
13 July 2000	0917:30	87.8	30
11 August 2000	1810:30	6.6	7
14 August 2000	2135:30	-62.9	-30
15 September 2000	0407:00	-89.9	-6
17 September 2000	2343:30	-6.7	27
28 October 2000	0908:00	-15.8	-40
26 November 2000	1124:00	-86.8	13
31 January 2001	0723:00	-44.8	0
18 April 2001	0004:30	2.2	11
17 August 2001	1016:00	-30.9	-40
27 August 2001	1919:00	26.8	22
21 October 2001	1612:30	63.4	16
25 October 2001	0802:30	35.7	24
19 November 2001	1735:00	-11.2	32
18 March 2002	1236:30	50.8	0
23 April 2002	0415:00	-25.1	0

Table 2: Plasma parameters at geosynchronous orbit for sub-auroral proton arc events.

Date	Event Time at IMAGE	LANL Spacecraft	Space craft MLT	A_h before	$\frac{V_h}{V_{th}}$ before	n_h/n_c before	A_h after	$\frac{V_h}{V_{th}}$ after	n_h/n_c after
14 Jun 2000	1435	1991-080	15.2	0.53	0.43	0.55	0.62	0.52	0.30
13 Jul 2000	0955	1991-080	10.7	0.46	1.12	0.08	0.55	0.80	0.09
15 Sep 2000	0453	1994-084	11.6	0.40	2.53	0.08	0.59	1.17	0.28
19 Sep 2000	0720	1994-084	14.2	0.28	0.77	0.21	0.37	0.99	0.15
8 Nov 2000	0614	1994-084	13.1	0.30	1.01	0.25	0.29	0.95	0.39
18 Apr 2001	0045	1991-080	13.3	0.54	1.14	0.09	0.54	1.54	0.10
11 Sep 2001	1558	01A	16.3	0.28	3.00	0.05	0.38	3.97	0.03
25 Oct 2001	0855	97A	13.5	0.46	0.47	0.38	0.47	3.21	0.06
25 Oct 2001	0855	1994-084	15.9	0.40	1.51	0.10	0.45	3.54	0.06
25 Oct 2001	0855	01A	9.4	0.64	2.96	0.05	0.63	5.38	0.04
12 Dec 2001	1345	01A	14.2	0.32	6.13	0.03	0.37	8.13	0.02

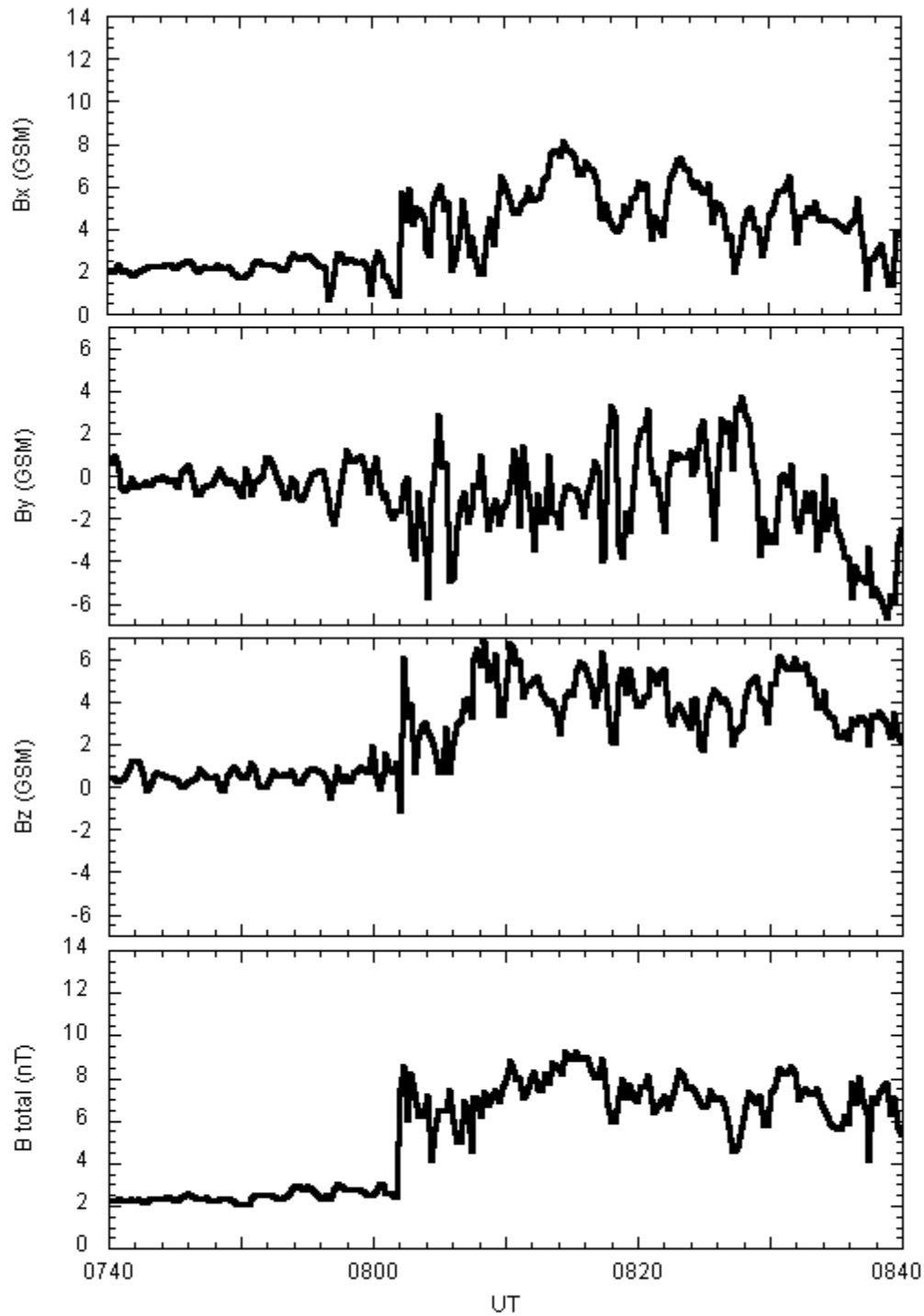


Figure 1: Magnetic field data from the ACE spacecraft on 25 October 2001. A strong interplanetary shock passed the spacecraft at 0802 UT. These data are used to compute the shock normal angle.

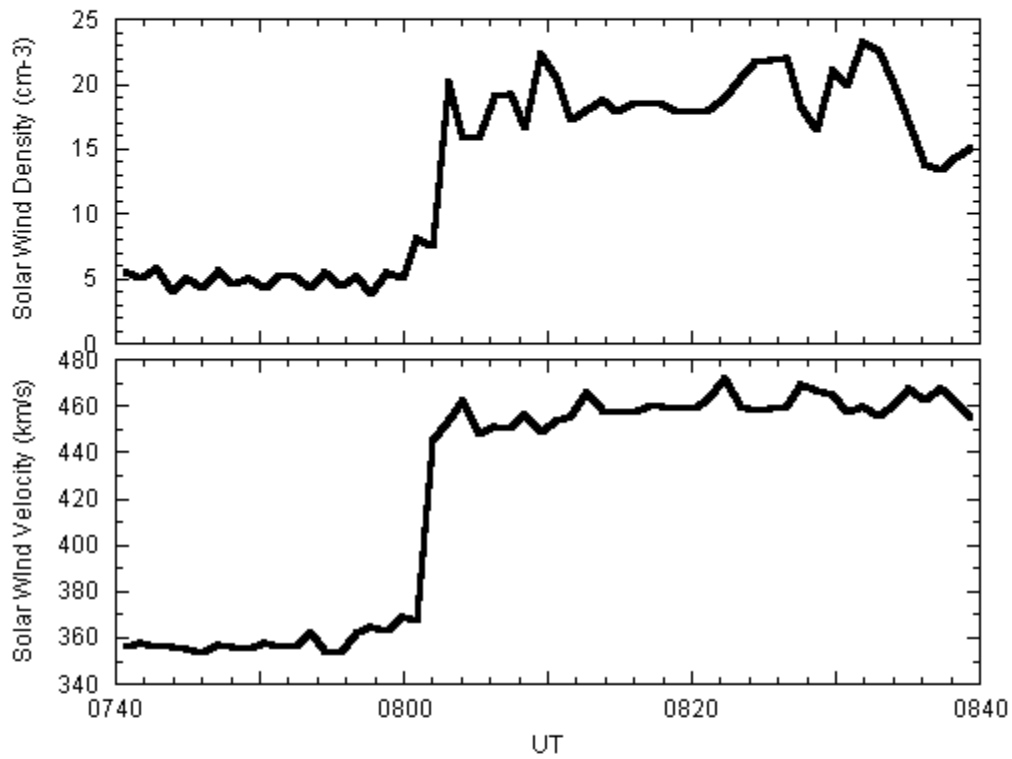


Figure 2: Plasma data from the ACE spacecraft on 25 October 2001. The solar wind velocity and density increase across the interplanetary shock. Using the downstream solar wind velocity, this shock arrived at the magnetopause approximately 50 min after the ACE spacecraft encounter.

Title:
C:\Documents and Settings\Claffier\My Documents\Fig1_20011025\image3.eps
Creator:
Jasc Software, Inc.
Preview:
This EPS picture was not saved
with a preview included in it.
Comment:
This EPS picture will print to a
PostScript printer, but not to
other types of printers.

Figure 3: IMAGE FUV data from 25 October 2001. The top panels show the Doppler-shifted Lyman Alpha emissions remapped into invariant latitude and magnetic local time. Noon is to the top and dusk is to the left. The auroral oval is at about 75° invariant latitude and the sub-auroral proton arc is at about 68° invariant latitude between 11 and 15 MLT in the 0855 UT image. In subsequent images, the sub-auroral arc splits, with one part propagating toward dusk and the other propagating toward dawn. Both parts tend to merge with the auroral oval. The bottom panels show the mapping of the FUV emissions from the ionosphere to the GSM equatorial plane. In the left-hand panel, the sub-auroral proton arc maps to a region between about 11 and 15 MLT and between about 5 and 8 R_E . In subsequent mappings, the arc splits and propagates around the dayside outer magnetosphere.

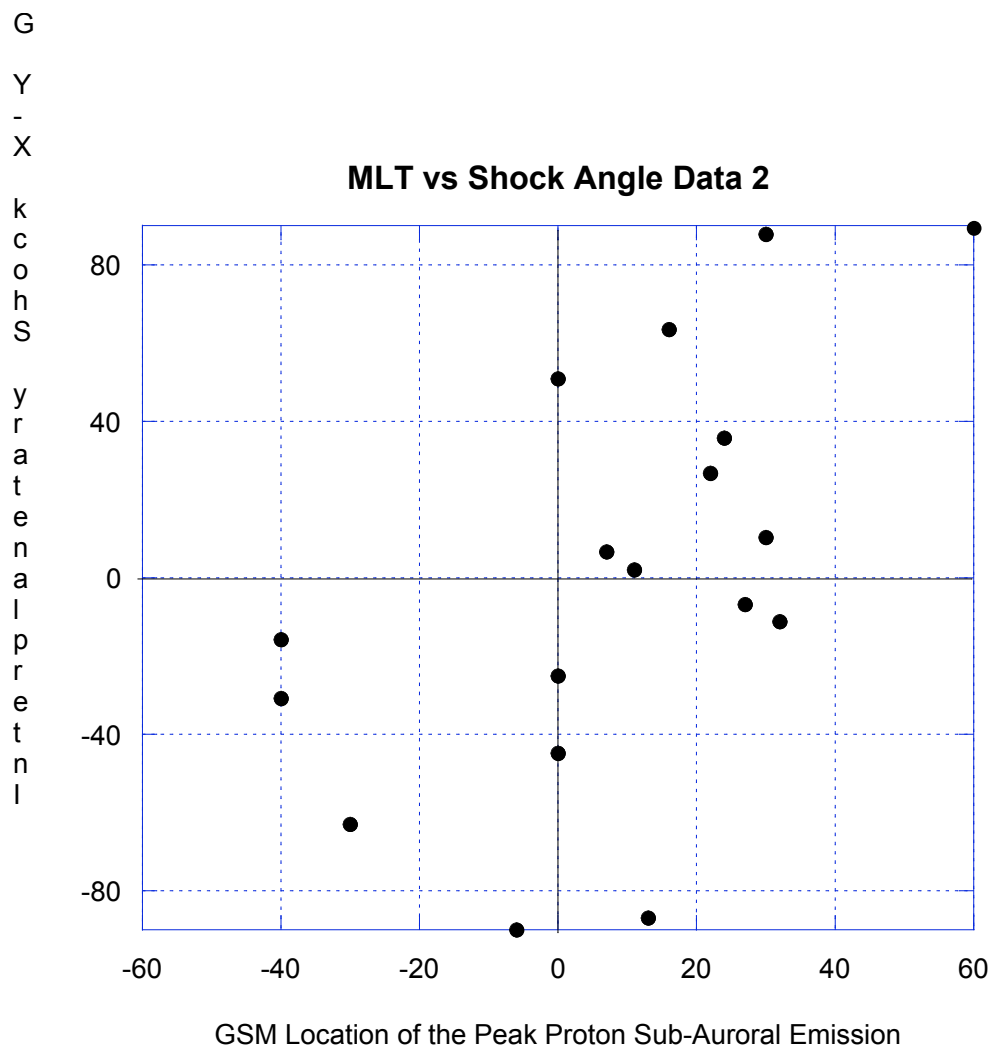


Figure 4: Interplanetary shock normal angle in the X-Y GSM plane versus the GSM location of the peak in the proton sub-auroral emissions. Although the correspondence is not one-to-one, there is a clear tendency for sub-auroral emissions to peak on the duskside (dawnside) when the shock normal has a positive (negative) YGSM component. That is, shocks that arrive at the duskside (dawnside) magnetopause tend to create sub-auroral proton arcs that peak on the duskside (dawnside).

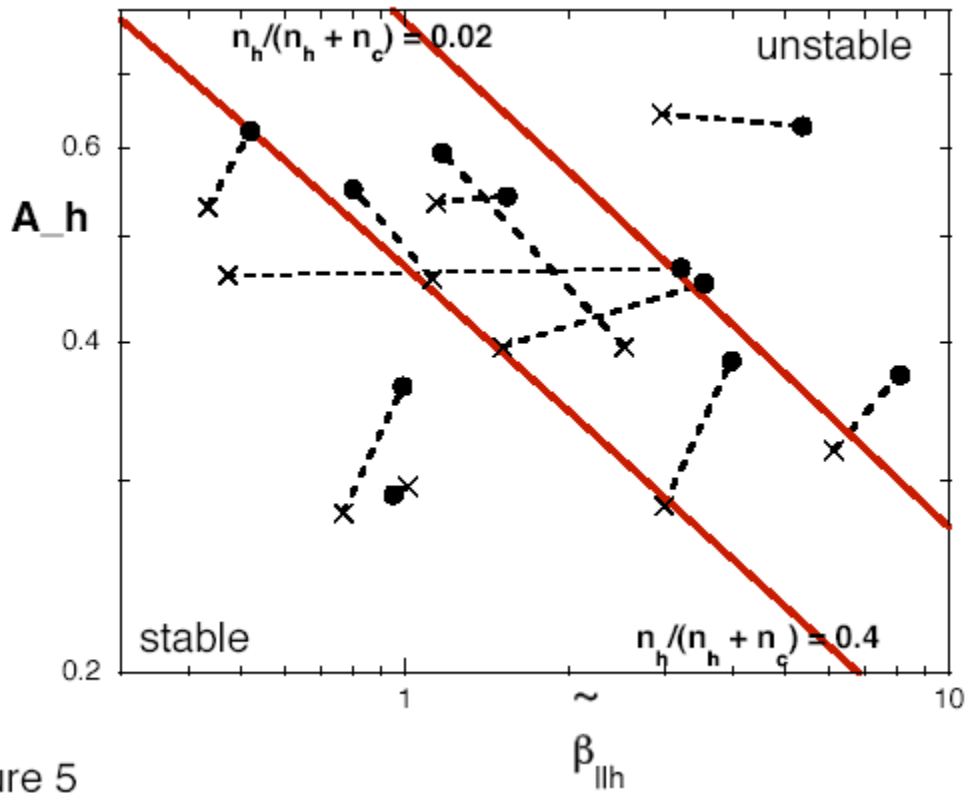
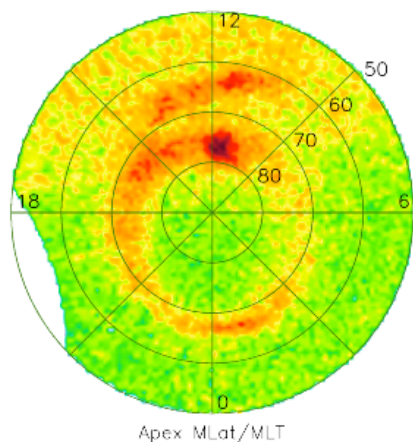


Figure 5

Figure 5. Modified hot plasma $\beta_{\parallel h}$ (including the cold plasma density) versus temperature anisotropy $A_h = (T_{\perp h}/T_{\parallel h} - 1)$ for 11 events before (\times 's) and after (\bullet 's) the compression of the magnetosphere. The plasma moves toward increasing instability due to this compression. On average, the points move more in $\beta_{\parallel h}$ than in A_h , indicating that changes in $\beta_{\parallel h}$ are more important than changes in A_h for the EMIC wave growth for most events.

IMAGE/FUV SI12

14 Jun 2000
1630



18 Apr 2001
0047

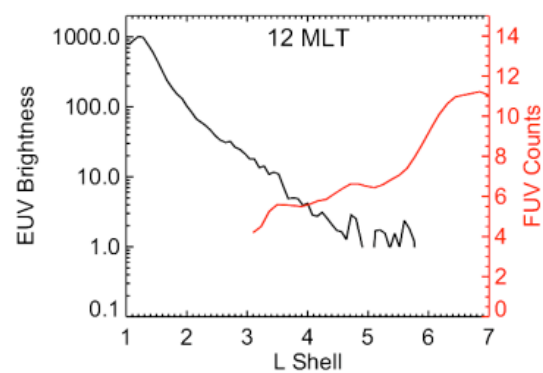
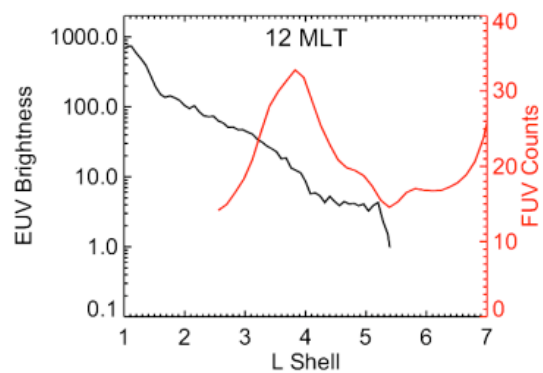
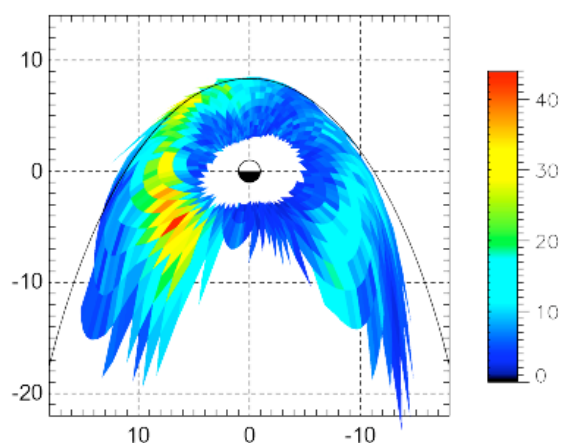
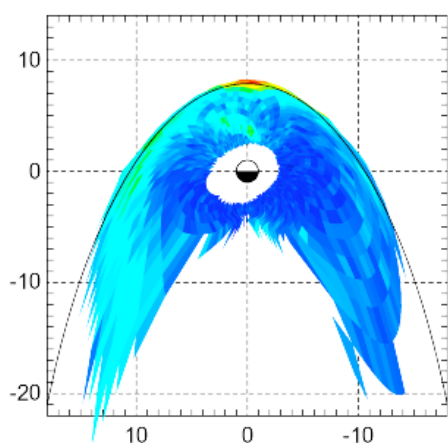
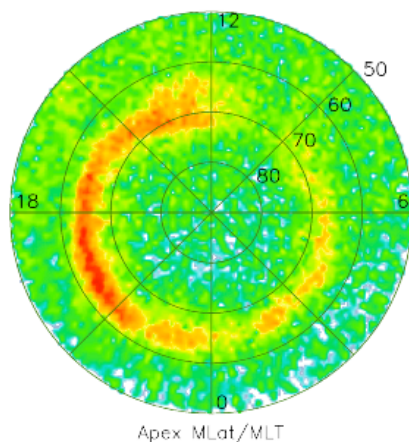


Figure 6. IMAGE FUV and EUV data from two sub-aurora proton events. The top and middle panels are similar to those in Figure 3. The bottom panels compare cuts in the proton precipitation mapped to the equatorial plane with similar cuts in the EUV He^+ emissions (proportional to the plasmaspheric density assuming a constant He^+/H^+ density ratio). For the event on 14 June 2000, (left hand panels) the sub-auroral proton arc is separate from the higher latitude auroral oval. Mapped to the equatorial plane, this arc occurs quite close to the Earth and extends from noon to the duskside. The sunward edge of the precipitation at 12 MLT compares well with the decrease in the plasmaspheric density at the plasmapause at 3.8 R_E . (The drop in the EUV brightness at 6 R_E is the edge of the EUV image). Thus, the growth of the EMIC waves that scatter the protons is controlled by the cold plasma density profile for this event. For the event on 18 April 2001 (right hand panels), there is no gap between the sub-auroral proton arc and the auroral oval emissions. These emissions extend inward from the magnetopause to inside geosynchronous orbit on the duskside. For this event, the cold plasma density appears anti-correlated with the mapped proton emissions. Thus, for this event, the EMIC wave growth is not dominated by the cold plasma density.